Acta Materialia 307 (2026) 121975

Contents lists available at ScienceDirect

Acta Materialia

journal homepage: www.elsevier.com/locate/actamat

Full length article

Field-driven magnetization processes, magnetocalloric effect and tunneling magnetoconductivity in bilayer CrI_3 thin films: Insights from replica-exchange Monte Carlo simulations

Phong H. Nguyen [a], Cong T. Bach [a], Huy D. Nguyen [a], Hoai T.L. Nguyen [b], Hanh H. Mai [c], Duy Q. Dao [d], Giang H. Bach [a,*]

[a] Faculty of Physics, University of Science, Vietnam National University, Hanoi, 334 Nguyen Trai Street, Thanh Xuan, Hanoi, Vietnam
[b] Institute of Physics, Vietnam Academy of Science and Technology, 10 Dao Tan Street, Hanoi, Vietnam
[c] Faculty of Electronics and Telecommunications, University of Engineering and Technology, Vietnam National University, Hanoi, 144 Xuan Thuy Street, Hanoi, Vietnam
[d] Faculty of Advanced Technology and Engineering, Vietnam-Japan University, Vietnam National University, Hanoi, Luu Huu Phuoc Street, My Dinh 1, Hanoi, Viet Nam

ARTICLE INFO

Keywords:
First-order magnetization process
Honeycomb spin lattice
CrI_3-like structures
Monte Carlo simulation
The Ising model
Magnetocaloric effect
Tunneling magnetoconductivity

ABSTRACT

We employ replica-exchange Monte Carlo simulations of Ising model for a bilayer honeycomb spin lattice with S = 3/2 to investigate field-driven magnetic behavior and first-order magnetization processes (FOMPs). The simulations reveal a step-like field dependence of the magnetic moment at low temperatures with a sudden saturation, occurring at a critical field h_c that linearly varies with interlayer coupling J_z. Without a magnetic field, an interlayer antiferromagnetic alignment is confirmed below the Néel temperature T_N for arbitrary interlayer coupling J_z, with T_N decreasing as the interlayer coupling strength $|J_z|$ weakens. We further analyzed the temperature dependence of layer-resolved magnetic moments, thermodynamic quantities and their relations to the magneto-caloric effect, where the magnetic entropy change $-\Delta S_M$ exhibits a double-peak structure in systems with competing AFM and FM interactions. Finally, we calculate the field dependence of the relative magnetoconductivity and compare it with experimental measurements, clarifying the intimate relationship between FOMPs and tunneling magnetoconductivity in bilayer CrI_3 thin films.

1. Introduction

Two-dimensional (2D) materials with honeycomb lattices have newly exhibited a range of intriguing physical properties, including novel electronic structures and emergent electric and magnetic behaviors [1]. Among these, magnetism in 2D van der Waals (vdW) materials has emerged as a central research focus. According to the Mermin–Wagner theorem, long-range magnetic order is forbidden at finite temperatures in isotropic Heisenberg models, due to the enhancement of quantum and spatial fluctuations in conjunction with thermal fluctuations [2]. However, recent experimental works have shown that magnetic order can be stabilized in 2D vdW heterostructures under external magnetic fields, challenging this limitation and opening new avenues for applications in spintronics, magneto-optoelectronic devices, and magnetic sensors [3–5].

Magnetic anisotropy is essential for stabilizing long-range magnetic order in 2D systems [4,6]. Experimental observations have indicated that reducing bulk materials to the monolayer or few-layer limit enhances magnetic anisotropy, along with modifying exchange interactions at low fields. As a result, intrinsic ferromagnetism has been observed in atomically thin layers of pristine $Cr_2Ge_2Te_6$ [4]. In contrast, the CrI_3 layered semiconductor exhibits a more complex magnetic behavior, characterized by interlayer antiferromagnetic (AFM) coupling coexisting with intralayer ferromagnetic (FM) order [3,7]. Since each magnetic layer is treated as a spin-polarized layer in nanostructure tunneling junctions, magnetic alignment in different 2D vdW layered materials plays a crucial role in determining transport properties, for example, the tunneling magnetoresistance (or tunneling magnetoconductivity) in spin filters [8–11].

In addition to the intrinsic properties of magnetic materials, tunneling magnetoresistance (TMR) is strongly influenced by external parameters such as magnetic field and temperature. At low temperatures, magnetic-field–controlled tunneling in few-layer CrI_3 thin films resembles the step-like behavior of the magnetization curve with plateaus

* Corresponding author.
E-mail address: gbach@hus.edu.vn (G.H. Bach).

https://doi.org/10.1016/j.actamat.2026.121975
Received 21 October 2025; Received in revised form 27 January 2026; Accepted 28 January 2026
Available online 2 February 2026
1359-6454/© 2026 Acta Materialia Inc. Published by Elsevier Inc. All rights are reserved, including those for text and data mining, AI training, and similar technologies.

corresponding to distinct interlayer spin configurations with parallel and antiparallel alignments. The emergence of staircase-like features referring to the first-order magnetization process (FOMP) is governed by some elements, including the number of CrI_3 layers, spin states, and the underlying magnetic interactions. Owing to this rich and tunable magnetic structure, bilayer CrI_3 thin films serve as versatile building blocks for spintronic devices. A detailed microscopic understanding of the interplay among spin dynamics and these elements is therefore essential for assessing and optimizing their potential for practical applications [8,12].

Theoretical studies employ models and simulations to achieve an in-depth understanding of the magnetic behavior and phase transitions in vdW layered materials. First-principles calculations of the electronic band structure of a semiconductor at zero temperature, specifically CrI_3 in different stacking configurations, reveal a consistent total magnetic moment of $3\mu_B$ [12–14]. This corresponds to the spin S = 3/2 of the Cr^{3+} ion aligning with Hund's rule. However, alternative computational approaches are required to overcome the inherent constraints of first-principles methods at finite temperatures. These include spin dynamics and Monte Carlo simulations that provide insight into the dynamic nature of magnetic behavior under an external field for bilayer CrI_3, offering a direct comparison with experimental observations.

Monte Carlo simulations have proven to be highly effective in describing the magnetic behavior and phase transitions of spin systems under external fields at finite temperatures, especially for illustrating the FOMP [15–18]. However, applications to bilayer graphene-like spin structures such as CrI_3 thin films are underexplored, as the commonly used Metropolis algorithm fails to accurately capture the magnetic phase transition at the critical field. To address this limitation arising from single-spin–flip dynamics, the replica-exchange method provides an efficient solution, enabling cluster-flip processes particularly in external fields that are essential for correctly sampling first-order phase transitions [6,19].

Our previous work employing a mean-field approximation [20] revealed the emergence of an intermediate step in the field-dependent magnetization, in addition to the saturation plateau. Such a feature, however, has not been observed experimentally in bilayer CrI_3 [3,8], raising important questions regarding the limitations of mean-field theory in capturing the true nature of the field-driven magnetization process. Motivated by this discrepancy, we undertake a comprehensive study of field-induced first-order magnetization processes (FOMPs) in order to validate the physical mechanisms governing these transitions and to accurately determine the critical field. To achieve this, we employ replica-exchange Monte Carlo simulations applied to the Ising model on a bilayer honeycomb lattice with spin $S = 3/2$. This model, with in-plane and out-of-plane anisotropic exchange interactions, provides a minimal yet effective framework for describing the magnetic properties of CrI_3 systems.

Beyond magnetization processes, we further explore the intimate connection between the magnetocaloric effect and the underlying magnetic behavior. This is accomplished by calculating the magnetic entropy change as a function of interlayer coupling, thereby elucidating how entropy variations reflect the competition between AFM and FM arrangement. Moreover, we extend our analysis to transport properties by determining the field dependence of tunneling magnetoconductivity and directly comparing the results with available experimental data. This comparison not only clarifies the correlation between FOMP behavior and tunneling magnetoconductivity but also highlights the significance of field-tunable spin configurations in bilayer CrI_3 for potential spintronic applications.

2. Model and calculation method

We study the spin S = 3/2 Ising model on a bilayer honeycomb lattice consisting of $2N$ sites, where $N = L \times L$ is the number of sites in each layer, with intralayer coordination number $\boldsymbol{q = 3}$, as illustrated in Fig. 1. The system employs periodic boundary conditions along the x and y directions and open boundary conditions along the z direction. The Hamiltonian is given by:

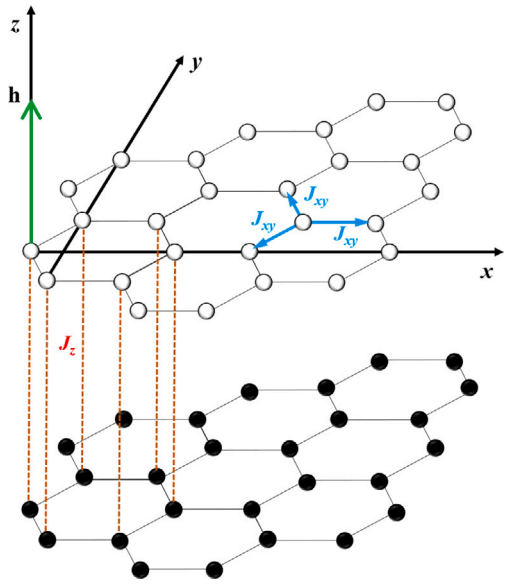


Fig. 1. Schematic representation of the bilayer honeycomb spin lattice in the S = 3/2 Ising model under an external magnetic field applied perpendicular to the layers. The open circles denote sites in the upper layer, while the filled circles correspond to sites in the lower layer. J_{xy} indicates the intralayer exchange coupling between nearest neighbors in each layer, and J_z represents the interlayer exchange coupling between the two layers.

$$H = -J_{xy} \sum_{\langle i,j \rangle} \sum_{v=a,b} S_{iv}^z S_{jv}^z - J_z \sum_i S_{ia}^z S_{ib}^z - h \sum_i \sum_{v=a,b} S_{iv}^z. \quad (1)$$

Here, a (b) is the upper (lower) layer index, S_{ia}^z (S_{ib}^z) denotes the z-component of a classical spin S = 3/2 at site i of the upper (lower) layer, with possible values $\pm 3/2$ and $\pm 1/2$. J_{xy} and J_z are the exchange coupling constants for the intralayer nearest neighbors $\langle i, j \rangle$ and interlayer neighbors (ia, ib), respectively. The last term accounts for the external (out-of-plane) magnetic field h, applied perpendicular to the spin layers.

Throughout this work, we use J_{xy} as a unit of energy and k_B as a unit of entropy. Under this choice, the parameters J_z, h, the internal energy E, and the temperature T are expressed in dimensionless form. As an illustration, the dimensionless temperature is defined as $T = k_B\tau/J_{xy}$, with τ representing the absolute temperature in Kelvin.

To resolve the slow relaxation in vdW heterostructures at low temperatures, we employ the parallel tempering (replica exchange) method [21]. In this approach, each replica evolves through local spin–flip updates that follow the Metropolis algorithm [22], while configuration exchanges between replicas are periodically attempted. This strategy enables the system to overcome energy barriers more effectively, since thermal fluctuations from replicas at higher temperatures can be transferred to those at lower temperatures. We do not apply the cluster hybrid algorithm used in our recent work [6], since the external field present in most of our results breaks the global spin–flip symmetry and renders cluster updates inefficient [23–25]. With a carefully chosen set of replica temperatures, the replica exchange method can reproduce the collective spin–flip behavior of cluster algorithms without being hindered by the external field, as will be demonstrated in Section 3. Furthermore, the replica exchange approach provides a reliable framework for revealing the intrinsic properties of bilayer spin systems in vdW heterostructures, while single-spin flip techniques such as the Metropolis or heat-bath algorithms, which have been applied in earlier studies [15–17,26–33], are not sufficient. This will also be verified in Section 3.

We investigate bilayer lattices of linear sizes $L = 30, 60, 90, 120$, and 180. The overall simulation procedure is organized in two main stages.

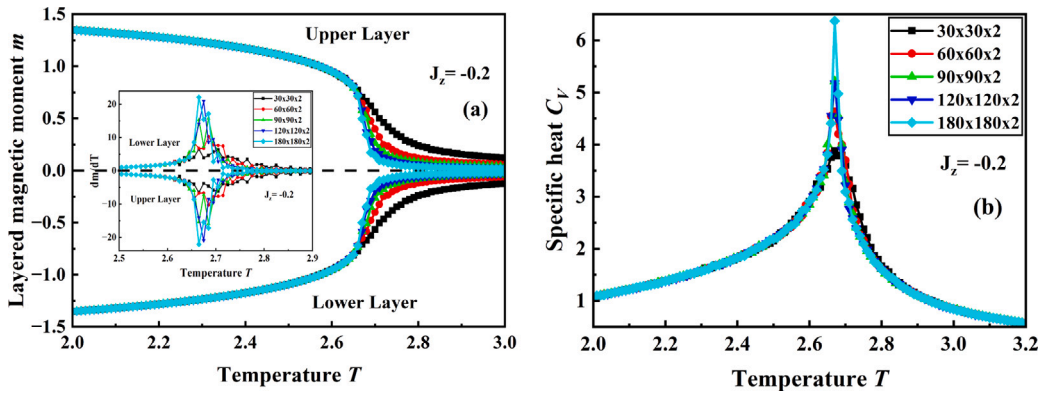


Fig. 2. Temperature dependence of the magnetic moment in each layer [upper layer (upper panel), lower layer (lower panel)] (a), and the specific heat (b) for different system sizes with parameters $J_z = -0.2$ and $h = 0$.

In the first stage, we perform conventional Monte Carlo simulations using the Metropolis algorithm combined with simulated annealing to identify effective temperature ranges and approximate transition temperatures. Starting from random spin states at high temperature, the system is gradually cooled, with the final configuration at each step serving as the initial state for the next. This gradual cooling ensures that the system remains close to equilibrium. At each temperature, 3×10^5 Monte Carlo sweeps are used for thermalization, followed by 10^6 sweeps for averaging thermodynamic observables.

In the second stage, once the approximate transition temperature T_c is estimated, we choose $N_T = 40$ temperatures T_i uniformly distributed between $T_{\min}$ and $T_{\max}$, where $T_{\max} > T_c$. Parallel simulations are then performed at these temperatures. During the process, about 10^5 exchange attempts are made between neighboring replicas. A configuration exchange between two replicas at inverse temperatures $\beta_i = 1/T_i$ and $\beta_{i+1} = 1/T_{i+1}$ is accepted with probability $P(\beta_i \Leftrightarrow \beta_{i+1}) = \min\{1, \exp(\Delta\beta\,\Delta E)\}$, where $\Delta\beta = \beta_{i+1} - \beta_i$ and $\Delta E = E_{i+1} - E_i$ are the differences in inverse temperatures and energies, respectively. Between consecutive exchange attempts, 100 Monte Carlo sweeps are performed, and the resulting data are used to compute ensemble averages of the thermodynamic quantities, which are [18]

Total energy per spin,

$$E = \frac{\langle H \rangle}{2N}, \tag{2}$$

Total magnetic moment per spin,

$$m = \frac{\langle \sum_{i=1}^{N} \sum_{v=a,b} S_{iv}^{z} \rangle}{2N}, \tag{3}$$

Magnetic moment per spin in each layer,

$$m_v = \frac{\langle \sum_{i=1}^{N} S_{iv}^{z} \rangle}{N}, \tag{4}$$

Total magnetic susceptibility per spin,

$$\chi = \frac{1}{4N^2} \frac{\langle (\sum_{i=1}^{N} \sum_{v=a,b} S_{iv}^{z})^2 \rangle - \langle \sum_{i=1}^{N} \sum_{v=a,b} S_{iv}^{z} \rangle^2}{T}, \tag{5}$$

Magnetic susceptibility per spin in each layer,

$$\chi_v = \frac{1}{N^2} \frac{\langle (\sum_{i=1}^{N} S_{iv}^{z})^2 \rangle - \langle \sum_{i=1}^{N} S_{iv}^{z} \rangle^2}{T}, \tag{6}$$

Specific heat,

$$C_V = \frac{1}{4N^2} \frac{\langle H^2 \rangle - \langle H \rangle^2}{T^2}, \tag{7}$$

Magnetic entropy per spin calculated in units of k_B,

$$S_M = \int_0^T \frac{C_V}{T} dT. \tag{8}$$

In studies of phase transitions, finite-size effects have an unignorable impact and must be carefully examined. To assess the reliability of the simulations, we vary the system size, as illustrated in Fig. 2. For relatively small lattices, such as $L = 30$ and $L = 60$, the magnitude of the magnetic moment in each layer decreases noticeably above the critical temperature when the system size increases. This is accompanied by a broad and strongly fluctuating inverse peak in the temperature derivative of the magnetic moment, dm/dT, as displayed in the inset of Fig. 2(a). In parallel, the corresponding specific heat exhibits a wide, weak, and noisy peak that gradually becomes sharper and higher as the lattice size grows. Such a broadened and diffusive peak is a characteristic manifestation of finite-size effects, since the system deviates from the thermodynamic limit where critical properties are well-defined [34,35]. For larger sizes, e.g., $L = 120$ and $L = 180$, further increases in the system size do not produce significant changes either in the magnetic moment behavior or in the shape and position of the specific heat's peak. Therefore, to balance computational cost and accuracy, we employ $L = 120$ in the subsequent simulations, which provides sufficient precision to extract physical properties, the critical temperature, and the critical external field.

3. First-order magnetization processes: Insight from replica exchange method.

We perform magnetic measurements using the Metropolis algorithm with different initial spin configurations. Fig. 3 shows the dependence of the total magnetic moment m on the external magnetic field h for two cases: a random initial configuration in Fig. 3(a) and a specific initial configuration consisting of a ferromagnetic layer with spin $S^z = 3/2$ and another layer with spin $S^z = -3/2$ in Fig. 3(b), evaluated at various temperatures. The results reveal distinctly different step-like features. In Fig. 3(a), a magnetization plateau around $m = 0.4$ emerges at low temperatures where $T \leq 0.1$, corresponding to a spin-flop state with $S^z = \pm 1/2$. In contrast, this feature is nearly absent in the case of a specific layered configuration. These observations suggest that the Metropolis algorithm is highly sensitive to the choice of initial configuration and may converge to metastable states, failing to reach the true equilibrium due to trapping in local energy minima.

To accurately locate the critical point of the vdW bilayer, we employed replica exchange Monte Carlo to overcome the ergodic issues inherent in single-spin-flip Metropolis dynamics. Using the same parameters as in Fig. 3, the magnetic moment m consistently converges across various initial configurations and random seeds, as shown in Fig. 4(a). In the low-temperature regime where $T \leq 1.0$, the total magnetic moment exhibits a sharp field-induced transition from a nonmagnetic state to full saturation at $m = 3/2$ when the external magnetic field reaches a critical threshold h_c. The threshold field, estimated as $h_c \approx |J_z S_{max}^z| \approx 0.3$ with $S_{max}^z = 3/2$, corresponds to the energy required to

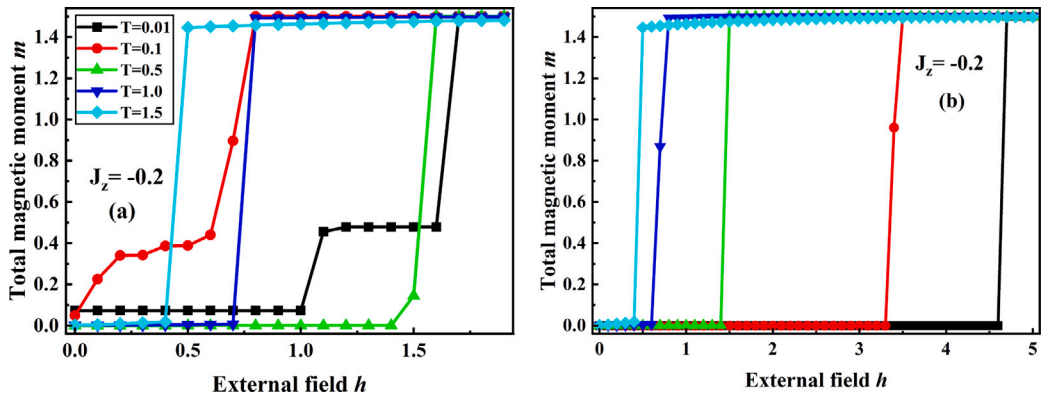


Fig. 3. Temperature dependence of total magnetic moment with an initial (a) random configuration and (b) AFM alignment of FM layers in the Metropolis algorithm.

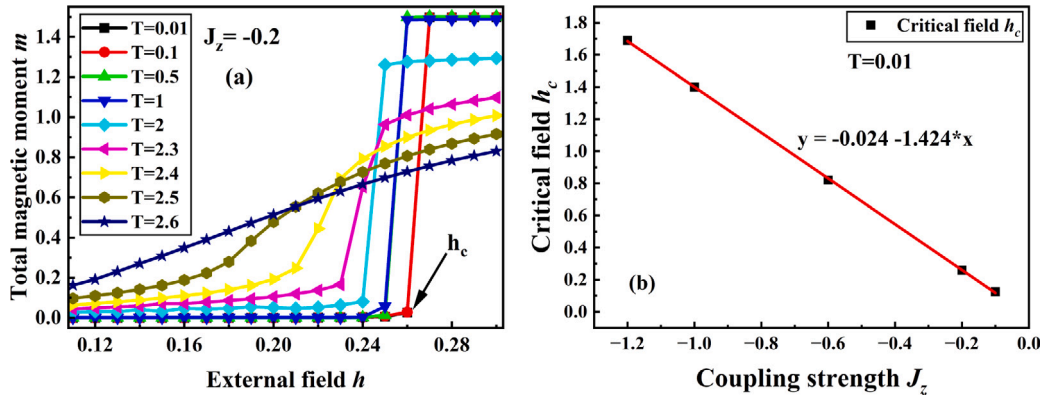


Fig. 4. (a) Temperature dependence of total magnetic moment using replica exchange method for interlayer coupling strength $J_z = -0.2$; (b) The dependence of critical field h_c on interlayer coupling strength J_z at temperature $T = 0.01$.

simultaneously flip all spins within a single layer. This collective nature of the spin reversal explains the failure of the Metropolis algorithm to accurately capture the critical field at low temperatures, as illustrated in Fig. 3 where $h_c \approx |qJ_{xy}S^z_{max}| + |J_z S^z_{max}|$ is strong enough to dominate the exchange energy of all nearest neighbors instead of interlayer coupling.

With increasing temperature, thermal fluctuations reduce the critical field and smear the transition, leading to a continuous and smooth evolution of the magnetic moment rather than an abrupt step. Notably, in the intermediate temperature regime, $1.0 < T < 2.3$, approaching the critical temperature T_N, the magnetic moment cannot saturate immediately above the critical field due to thermal fluctuations preventing long-range ferromagnetic order within each layer and fragmenting it into smaller ordered clusters.

Since the interlayer coupling J_z affects the persistence of the critical field h_c, we calculated the magnetization process for a range of J_z values to accurately extract h_c at $T = 0.01$, as shown in Fig. 4(b). The resulting linear relationship is highly compatible with the predicted scaling $h_c \approx |J_z S^z_{max}|$. Specifically, the fitted slope of 1.4(2) is in close quantitative agreement with the expected value of $S^z_{max} = 1.5$. This strong correspondence provides compelling evidence that AFM interlayer coupling is the dominant mechanism governing the observed FOMP in the bilayer spin systems.

Another key advantage of the replica exchange method is its ability to generate reliable energy and magnetic moment histograms at certain temperatures. This capability is crucial for identifying the nature of the phase transition. As shown in Fig. 5, both histograms exhibit a characteristic double-peak structure at temperature $T = 2.0$ and critical field $h_c = 0.24$, using the same parameters as in Fig. 4, providing clear evidence of the FOMP [6].

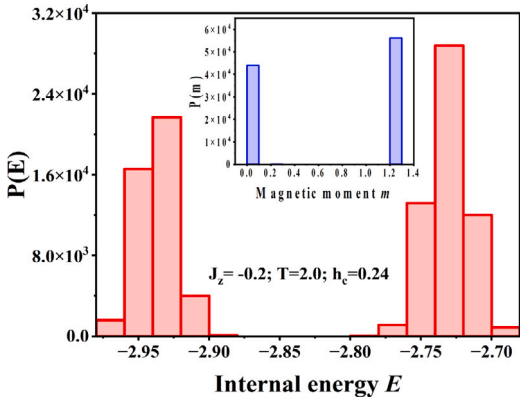


Fig. 5. Distribution function of internal energy (E) and magnetic moment m (see the inset) for $J_z = -0.2$, $T = 2.0$, $h_c = 0.24$.

4. Magnetic phase transition without external fields

To better understand the in-depth magnetic behavior of the bilayer film, we analyze the temperature dependence of the magnetic moment in each layer for various values of the coupling constant J_z, as shown in Fig. 6(a). The strong ferromagnetic (FM) intralayer interaction stabilizes FM ordering within each layer up to a common critical temperature defined by the position of sharp peak in the dm/dT and the spin susceptibility χ presented in Fig. 6(b)–(c) respectively.

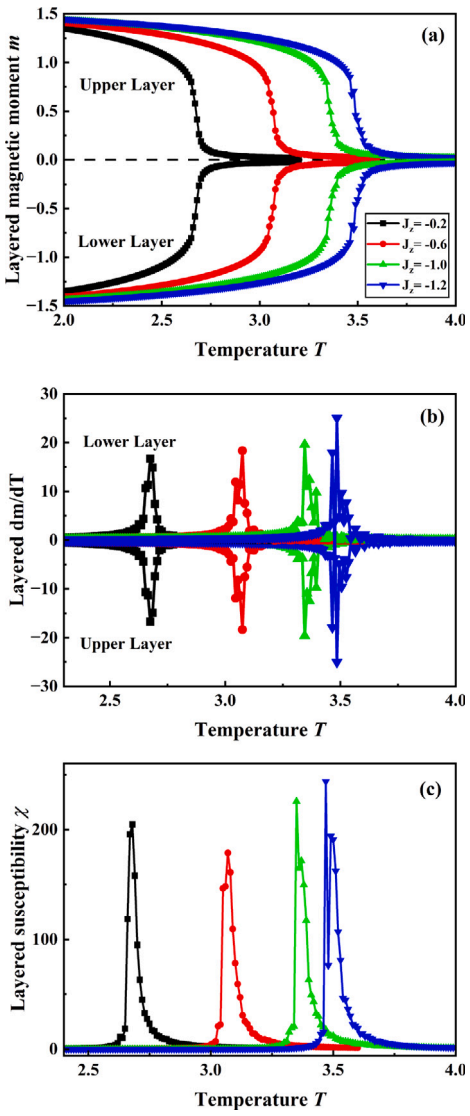


Fig. 6. Temperature dependence of layers' magnetic moment (a), their first derivative (b) and their spin susceptibility (c) with different interlayer couplings J_z.

For an interlayer antiferromagnetic (AFM) coupling ($J_z = -1.2$), layer-resolved magnetic moments adopt antiparallel alignment indicated by the opposite signs of their magnetic moments with exactly same values. This renowned behavior signals an AFM-to-PM phase transition through a Néel temperature T_N. This AFM arrangement prevails as long as the interlayer coupling J_z is present, although the critical temperature T_N shifts to lower temperatures when decreasing interlayer coupling strength $|J_z|$.

We also examine the dependence of total energy and specific heat on temperature displayed in Fig. 7 with varying J_z values. The energy curve in Fig. 7(a) that gradually increases through the critical temperature confirms the stability of the AFM state at low temperatures due to its lower energy compared to the energy in the PM state at high temperatures. The Néel temperature clearly realized by the maximum peak of the specific heat is coincident with the previously determined T_N. Furthermore, the specific heat analysis provides insight into the nature of the transition. Consistent with our recent findings [6], where the specific heat of a first-order magnetic transition (FOMT) is significantly larger than that of a second-order magnetic transition (SOMT), the observed features indicate that the AFM-to-PM phase transition in the bilayer system is evenly a SOMT for all interlayer couplings.

Using a mean-field approximation (MFA), the Néel temperature can be estimated as $T_N \approx q|J_{xy}| + |J_z|$, representing the thermal energy required to completely disrupt the exchange interactions between nearest-neighbor spins, thereby driving the system into a paramagnetic state. For this reason, a stronger interlayer coupling $|J_z|$ leads to a higher Néel temperature T_N. From the computational perspective, we extract the change of T_N with varying $|J_z|$ as illustrated in Fig. 8 to benchmark our results against the MFA calculation. In the strong-coupling regime, T_N exhibits an approximately linear dependence on $|J_z|$, in qualitative agreement with the MFA prediction. The extracted slope is about 0.8, which is smaller than the MFA value of 1.0. This overestimation is expected as spin fluctuations are neglected within the MFA but are fully captured in our simulation. Moreover, this analysis accounts for the relatively high calculated Néel temperature of the bilayer system $T_N \approx 2.28$ even with a negligible interlayer AFM coupling ($|J_z| = 0.001$), in which a nonlinear dependence of T_N on $|J_z|$ has emerged instead. The deviation reflects the complexity of the system in the weak coupling regime, where each layer hosts numerous large coexisting FM and AFM clusters with different S^z values. This approximated relation highlights the interplay between intra- and inter-layer interactions in determining the delicate balance of thermal stability and magnetic ordering of the spin system.

5. Magnetic phase transition with external fields

5.1. Magnetic behaviors

The response of the bilayer honeycomb spin lattice to an external magnetic field is illustrated in Fig. 9. For an interlayer coupling $J_z = -0.01$, the layer-resolved magnetic moment closely follows the zero-field behavior at very low fields $h < 0.0075$, where the antiferromagnetic alignment persists throughout the system (see Fig. 9(a)). This evolution is consistent with the total magnetic moment presented in Fig. 9(b), which remains relatively small and exhibits a slight anomaly near the critical temperature.

Interestingly, the layer-resolved magnetic moment exhibits a pronounced anomaly at a certain field $h = 0.0075$ (shown with green triangle-point lines). At $T \approx 2.3$ (near the Néel temperature T_N in Fig. 8), the magnetic moment of the lower layer abruptly switches from negative to positive, merging with that of the upper layer. This sudden reversal leads to a sharp maximum in the total magnetic moment near T_N (Fig. 9(b)), reflecting a simultaneous spin–flip transition in the lower layer that establishes a ferromagnetic alignment of both layers. The resulting FM state is subsequently destroyed upon heating to a higher critical temperature T^*. The sign of dm/dT, shown in the inset, further distinguishes FM-to-PM (− sign) from AFM–to-PM (+ sign) transitions in the bilayer system. At high fields, the temperature dependence of the layer-resolved magnetic moments exhibits only an FM–to-PM transition, characterized by a broad high-temperature tail.

We further analyze the temperature dependence of the internal energy E (Fig. 10(a)) and specific heat C_V (Fig. 10(b)) under applied magnetic fields for the case $J_z = -0.01$. While the external field has little effect on E across all temperatures, low fields strongly impact C_V near the Néel temperature, indicated by a sharply enhanced peak, signaling the change in internal energy at the transition. These features are fully consistent with the former magnetic response.

5.2. Magnetocaloric effect

The magnetocaloric effect is directly linked to the magnetic entropy change of the bilayer spin system under different external fields, which is defined as $-\Delta S_M(h,T) = S_M(0,T) - S_M(h,T)$. Figs. 11(a)–(c) show the magnetic entropy change $-\Delta S_M$ as a function of temperature for various field strengths and interlayer couplings $J_z = -0.001$, -0.01, and -0.1, respectively. At low fields ($h < h_c$), $-\Delta S_M$ exhibits two distinct maxima at temperatures coinciding with those of dm/dT in the inset of

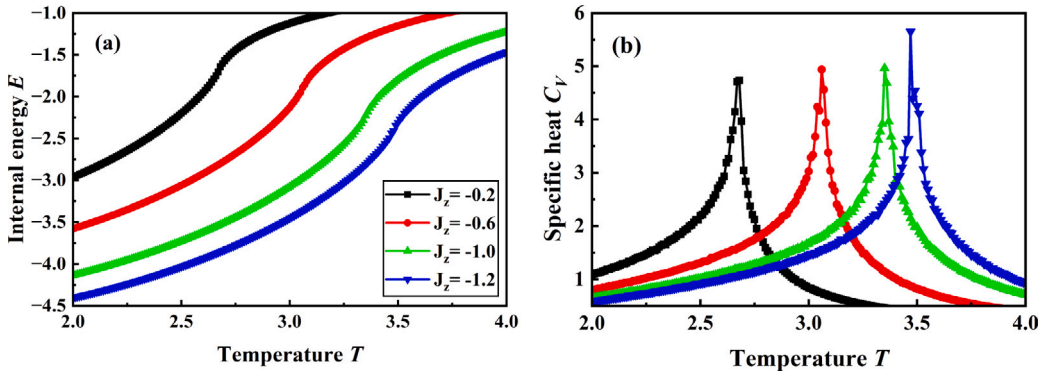


Fig. 7. Temperature dependence of internal energy (a) and specific heat (b) with different interlayer couplings J_z.

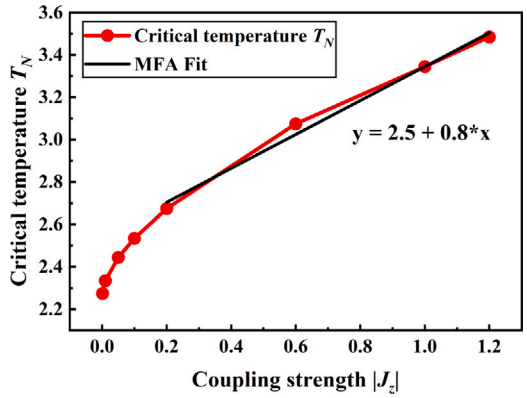


Fig. 8. The dependence of critical temperature T_N on interlayer couplings $|J_z|$ in comparison with linear fitting suggested by mean field approximation (MFA) in the strong coupling regime.

Fig. 9(b). The lower-temperature peak corresponds to the AFM–to-FM transition, whereas the higher-temperature peak marks the FM–to-PM transition upon heating. Similar double-peak behavior has been reported in magnetic systems with competing AFM and FM exchange interactions, commonly referred to as reentrant magnetism [36,37]. Although analogous structures have been recently observed in CrI_3 bulks, their microscopic origin remains unresolved [14].

The opposite signs of these peaks reflect contrasting magnetic responses: the AFM-to-FM transition increases spin disorder, whereas the FM-to-PM transition enhances spin alignment under the applied low field. Moreover, the redistribution of their weights with changing field reveals fluctuating spin disorder strength between these transitions. When the external field is larger than the critical field h_c where the system turns to ferromagnetism at low temperatures, the magnetic entropy change inherits a single peak at FM-to-PM critical temperature T^* as presented in blue solid lines in Fig. 11 for all interlayer coupling strengths.

5.3. Tunneling magnetoconductivity

Since the magnetic behavior of bilayer CrI_3 strongly influences its transport properties, for example, the spin-dependent tunneling current of electrons through these layers in spin-valve devices, we apply our results for the magnetic moment under an external magnetic field to examine the tunneling current. Using the spin-polarized tunneling theory for granular materials described in detail in Refs. [37,38], tunneling relative magnetoconductivity G_r is given by

$$G_r = \frac{G(T,h)}{G(T,0)} = 1 + P^2\left(\frac{m}{m_0}\right)^2, \tag{9}$$

with magnetic moment of spin systems m and saturated magnetic moment m_0. The spin polarization of incident electrons interacting with localized spins of honeycomb lattices can be approximated,

$$P = \frac{n_\uparrow - n_\downarrow}{n_\uparrow + n_\downarrow} = \tanh\left[\frac{J_H}{T}\left(S + \frac{1}{2}\right)\right], \tag{10}$$

with Hund interaction J_H, defined in terms of J_{xy}, between localized spins $S = 3/2$ and tunneling electrons. We choose a constant $J_H = 3J_{xy}$ for the following calculations, assuming a strong interaction between them. For a graphite/bilayer CrI_3/graphite junction, the magnetoconductivity has an intimate relation to the TMR, which is [9],

$$\mathrm{TMR} = 100\% \times \frac{G(T,h) - G(T,0)}{G(T,0)} = 100\% \times (G_r - 1). \tag{11}$$

The recent experimental observation of a step-like dependence of tunneling current on out-of-plane magnetic field in bilayer CrI_3 thin film has prompted a detailed theoretical investigation. In Fig. 12, we present relative tunneling magnetoconductivity G_r derived in Eqs. (9)–(10). This calculation is compared with the experimental zero-bias tunneling current data for a bilayer CrI_3 film shown in red circles from Ref. [9]. It is worth noting that, for the hysteresis loops (see Fig. 2 A of Ref. [9]), we shift the origin of the magnetic field to the midpoint between the critical fields $\pm B_c$ for each magnetization direction, to fit with the reference used in our calculations, where the magnetization is initialized from the AFM state.

Our results demonstrate strong agreement with the experimental data, particularly in reproducing the existence of a critical field, h_c, at which both the relative magnetoconductivity, G_r, and zero-bias magneto-conductance (see Fig. 2 A in Ref. [9]), exhibit a sharp step-like jump. It should be noted that the relative tunneling magnetoconductivity G_r defined in Eq. (9) is primarily determined by the magnetic moment of the materials, since spin polarization P relating the tanh function in Eq. (10) rapidly saturates to unity when operating temperatures are much smaller than the Hund interaction J_H ($T \ll J_H$). Therefore, at $T = 0.02$, the appearance of G_r closely mirrors the step-like structure of the magnetization m, as a function of the magnetic field, (referring to the FOMP) displayed in the inset of Fig. 12 for an interlayer exchange coupling of $J_z = -0.05$. Quantitatively, the simulated conductivity increases by nearly a factor of two, equivalent to the TMR of about 100% following by Eq. (11), in excellent agreement with the experimental value of 95% [9]. It was further reported that the spin polarization of bilayer CrI_3 reaches approximately 85%, which aligns well with our earlier assumption of strong coupling between tunneling electrons and localized spins, leading to nearly full spin polarization of the tunneling current ($P \approx 1$) through the reduction of the tunneling barrier for one spin channel [39].

To estimate the energy scale in our model relative to the experimental values, we take the in-plane exchange energy as the energy unit, $J_{xy} = k_B\tau_N/T_N \approx 1.59$ meV, where $T_N \approx 2.44(5)$ for the chosen value

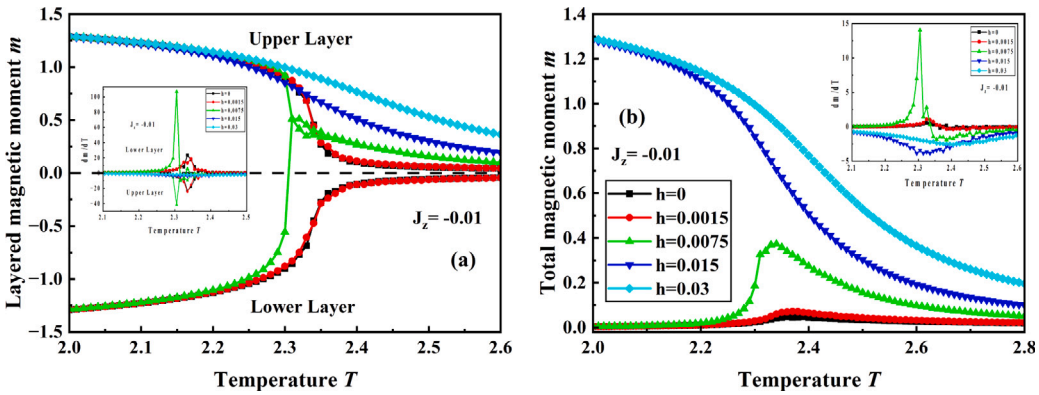


Fig. 9. Temperature dependence of layer-resolved (a) and bilayer (b) magnetic moment for the interlayer coupling intensity $J_z = -0.01$ at different field strengths. The insets show the dependence of dm/dT on temperature.

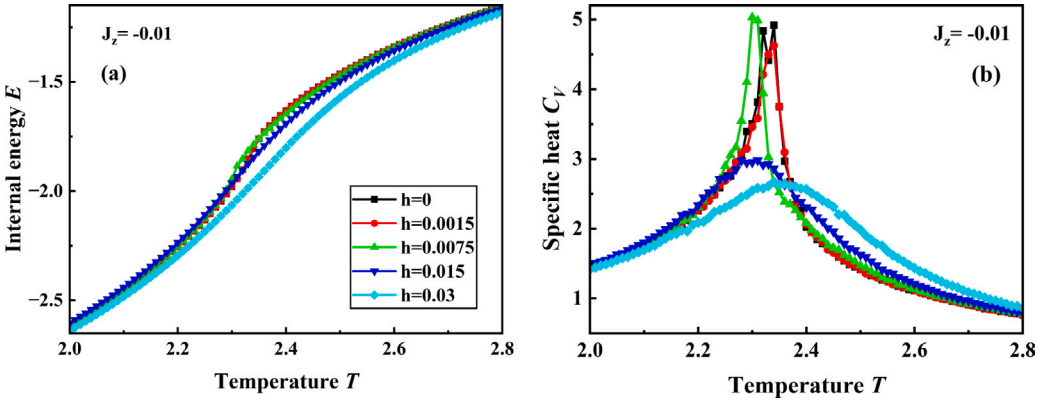


Fig. 10. Temperature dependence of internal energy (a) and specific heat (b) for interlayer couplings $J_z = -0.01$ at different field strengths.

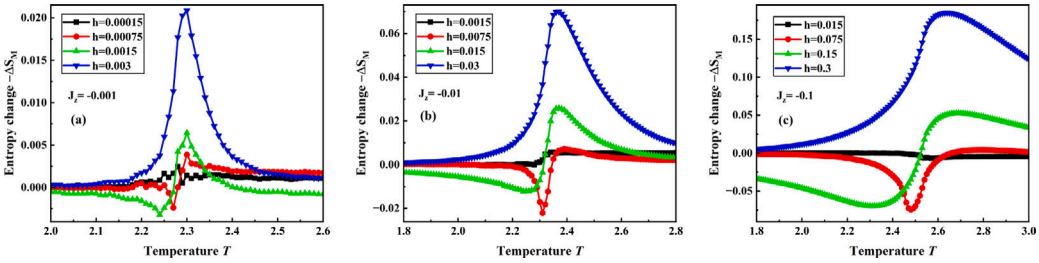


Fig. 11. Temperature dependence of magnetic entropy change for various interlayer couplings $J_z = -0.001$, -0.01, -0.1 at different field strengths, respectively.

of $J_z = -0.05$ in our model, extracted from Fig. 8. Here, $\tau_N = 45$ K corresponds to the Néel temperature of a CrI_3 monolayer (referred to range from 45 K to 61 K in bulk samples) [3,9]. The critical field is then obtained as

$$B_c = \frac{h_c J_{xy}}{g\mu_B} \approx 0.75 \text{ T},$$

using dimensionless field $h_c \approx 0.05(5)$ (see Fig. 12), and Landé factor $g = 2$. This value matches well with the measured field of approximately 0.65–0.7 T at low temperature 300 mK equivalent to $T \approx 0.02$, emphasizing the close correspondence between our theoretical modeling and the experimental observations [3,9].

In Table 1, we also compare our results with those obtained from other computational approaches, including density functional theory (DFT) associated with Metropolis Monte Carlo simulations, to estimate the interlayer-to-intralayer coupling ratio J_z/J_{xy}, the Néel temperature T_N, and the critical field B_c of bilayer and bulk CrI_3. DFT calculations based on the Vienna *ab initio* Simulation Package (VASP) [40] and Quantum ESPRESSO [41], as reported in Ref. [12], produce values of the dimensionless ratio J_z/J_{xy} in the range of -0.03 to -0.09, which are of the same order as our results (-0.05) for bilayer CrI_3. A corresponding increase in the Néel temperature T_N (often referred to as the critical temperature T_c) and a consistency of the experimental

Table 1
Comparison of interlayer-to-intralayer coupling ratio J_z/J_{xy}, Néel temperature T_N, and critical field B_c obtained from our replica-exchange Monte Carlo (REMC) simulations of bilayer (2L) CrI_3 described by the Ising model and from density functional theory (DFT) calculations combined with Metropolis Monte Carlo (MEMC) simulations based on Heisenberg models for bilayer and bulk CrI_3 [12,14].

Methods	J_z/J_{xy}	T_N (K)	B_c (T)	Ref.
DFT-MEMC for 2L CrI_3	−0.03	31	0.65	[12]
DFT-MEMC for 2L CrI_3	−0.07	34	0.65	[12]
DFT-MEMC for bulk CrI_3	−0.09	113	–	[14]
REMC for 2L CrI_3	−0.05	45	0.75	current work

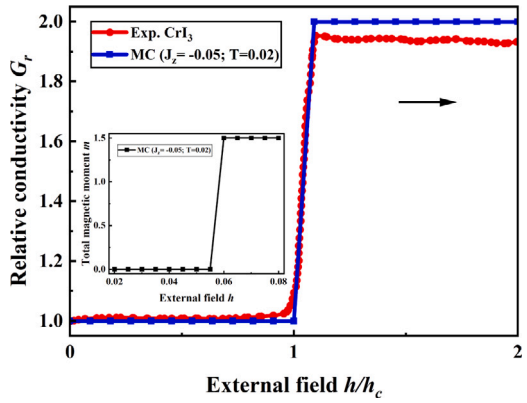


Fig. 12. Field dependence of relative magnetoconductivity (blue square) and total magnetic moment (inset) of the bilayer honeycomb spin lattice for interlayer coupling $J_z = -0.05$ at $T = 0.02$ in comparison with experimental observation for bilayer CrI_3 film in Ref. [9] (red circle). (For interpretation of the references to color in this figure legend, the reader is referred to the web version of this article.)

critical field B_c, which is about 0.65-0.7 T, have been found [3,9]. The remaining quantitative differences can be attributed to several factors: (i) the use of different exchange–correlation functionals in the DFT calculations; (ii) the neglect of long-range interactions in our model, in contrast to the inclusion of both nearest-neighbor and long-range interactions in Refs. [12,14]; and (iii) differences in the Monte Carlo methodologies employed to determine the critical temperature, namely the Metropolis algorithm used in Refs. [12,14] versus the progressive replica-exchange method adopted in the present work.

6. Conclusions

In summary, replica exchange Monte Carlo simulations of the Ising model demonstrate clear advantages in capturing the first-order magnetization process in a bilayer honeycomb spin lattice with spin quantum number S = 3/2. These simulations effectively reveal the strong influence of anisotropic exchange interactions in bilayer CrI_3 thin films, which exhibit FM spin alignment within each layer and AFM alignment between the layers.

Our results confirm these effects by examining the temperature-dependent behavior of both the layer-resolved and thermodynamic quantities of the bilayer system. The calculations reveal the Néel temperature, T_N, corresponding to the AFM-to-PM transition between layers in the absence of an external magnetic field. Notably, this magnetic order remains robust as long as the interlayer coupling J_z is finite, even if it is very weak. This persistence arises from the coexistence of strong FM interaction J_{xy} between in-plane nearest neighbors and interlayer AFM coupling, producing an approximate relation for the Néel temperature, $T_N \approx q|J_{xy}| + |J_z|$. The linear behavior of T_N on interlayer coupling has been found only in the strong coupling regime. Meanwhile, in the weak-coupling regime, deviations from linearity indicate that the magnetic behaviors of monolayer and bilayer systems are fundamentally distinct and cannot be reconciled merely by scaling interlayer coupling.

At low temperatures, the AFM alignment between layers is maintained under an applied external field. When the field strength reaches a critical value h_c at which spin flipping occurs, the total magnetic moment exhibits a step-like behavior, transitioning from 0 (reflecting AFM alignment) to 3/2 (indicating a fully saturated FM state), in line with the single-step observation of field-dependent magneto-optical Kerr rotation measurements in bilayer CrI_3 [3]. This critical field increases linearly with the interlayer AFM coupling strength $|J_z|$, approximately following by $h_c \approx |J_z S^z_{max}|$.

The magnetic behavior is closely tied to dynamic properties such as the magneto-caloric effect and tunneling magnetoconductivity. A key signature of the MCE in these systems is the emergence of a double-peak structure in the magnetic entropy change $-\Delta S_M$, characteristic of systems where FM and AFM phases compete. The negative and positive peaks correspond to the AFM-to-FM and FM-to-PM transitions, respectively. The magnitude of the MCE increases with stronger interlayer coupling, in agreement with observations in various doped perovskite materials that contain coexisting FM and AFM clusters.

Finally, tunneling magnetoconductivity resembles the magnetization process, with the tunneling current exhibiting a sharp onset at the critical field where the spins of one layer suddenly flip from $S^z_{min} = -3/2$ to $S^z_{max} = 3/2$, thus minimizing the system energy. This discontinuity corresponds to the step-like behavior of the magnetization m for an interlayer coupling of $J_z = -0.05$, with the double increase of simulated conductivity consistent with experiments. The observed spin polarization of about 85% supports our assumption of strong coupling between tunneling electrons and localized spins, leading to nearly full spin polarization of the current. By taking $J_{xy} = 1.59$ meV as the energy unit, the critical field is estimated as $B_c \approx 0.75$ T, in close agreement with the measured value of 0.65–0.70 T.

Supremely, the ability to efficiently modulate the tunneling current using very low magnetic fields spotlights the promising potential of bilayer CrI_3 films as an active element in spintronic technologies. In particular, the combination of atomic-scale thickness, large tunneling magnetoresistance (directly linked to tunneling magnetoconductivity), and field-tunable interlayer magnetic order makes bilayer CrI_3 an intriguing platform for ultrathin spin-filter tunnel junctions, nonvolatile magnetic memory devices, and spin-valve architectures [42,43]. The facile integration of CrI_3 into vdW heterostructures enables highly flexible and scalable 2D spintronic device designs [8,44,45]. Beyond spin transport, strong interdependence of spin, electronic, and optical response opens pathways toward optoelectronic devices where bilayer CrI_3 demonstrates gate-tunable magnetic states probed via magneto-optical Kerr microscopy [46].

CRediT authorship contribution statement

Phong H. Nguyen: Writing – original draft, Visualization, Validation, Methodology, Investigation, Formal analysis, Data curation, Conceptualization. **Cong T. Bach:** Writing – review & editing, Writing – original draft, Visualization, Validation, Supervision, Resources, Project administration, Investigation, Formal analysis, Conceptualization. **Huy D. Nguyen:** Investigation, Formal analysis. **Hoai T.L. Nguyen:** Software, Resources, Investigation, Conceptualization. **Hanh H. Mai:** Validation, Resources, Formal analysis. **Duy Q. Dao:** Resources, Investigation, Funding acquisition. **Giang H. Bach:** Writing – review & editing, Writing – original draft, Visualization, Validation, Supervision, Resources, Project administration, Methodology, Investigation, Funding acquisition, Formal analysis, Conceptualization.

Declaration of Generative AI and AI-assisted technologies in the writing process

During the preparation of this work we used ChatGPT in order to check grammars. After using this tool/service, we reviewed and edited the content as needed and take full responsibility for the content of the publication.

Declaration of competing interest

The authors declare that they have no known competing financial interests or personal relationships that could have appeared to influence the work reported in this paper.

Acknowledgments

The simulations are conducted using the High Performance Computing system of the Vietnam Academy of Science and Technology (VAST). This research is funded by the Vietnam National Foundation for Science and Technology Development (NAFOSTED, Vietnam) under grant number 103.02-2024.07 and the research project QG.24.101 of Vietnam National University, Hanoi. We thank Prof. Yoshitada Morikawa for valuable discussions and his generous hospitality at the University of Osaka.

References

[1] M.F. DiScala, D. Staros, A. de la Torre, A. Lopez, D. Wong, C. Schulz, M. Barkowiak, V. Bisogni, J. Pelliciari, B. Rubenstein, K.W. Plumb, Elucidating the role of dimensionality on the electronic structure of the Van der Waals antiferromagnet $NiPS_3$, Adv. Phys. Res. 3 (4) (2024) 2300096.
[2] N.D. Mermin, H. Wagner, Absence of ferromagnetism or antiferromagnetism in one- or two-dimensional isotropic Heisenberg models, Phys. Rev. Lett. 17 (22) (1966) 1133–1136.
[3] B. Huang, G. Clark, E. Navarro Moratalla, D.R. Klein, R. Cheng, K.L. Seyler, D. Zhong, E. Schmidgall, M.A. McGuire, D.H. Cobden, W. Yao, D. Xiao, P. Jarillo Herrero, X. Xu, Layer-dependent ferromagnetism in a van der Waals crystal down to the monolayer limit, Nature 546 (2017) 270–273.
[4] C. Gong, L. Li, Z. Li, H. Ji, A. Stern, Y. Xia, T. Cao, W. Bao, C. Wang, Y. Wang, Z.Q. Qiu, R.J. Cava, S.G. Louie, J. Xia, X. Zhang, Discovery of intrinsic ferromagnetism in two-dimensional van der Waals crystals, Nature 546 (7657) (2017) 265–269.
[5] M. Gibertini, M. Koperski, A.F. Morpurgo, K.S. Novoselov, Magnetic 2D materials and heterostructures, Nature Nanotechnology 14 (5) (2019) 408–419.
[6] P.H. Nguyen, N.T. Nguyen, H.D. Nguyen, H.T.L. Nguyen, C.T. Bach, G.H. Bach, Random-anisotropy driven giant magnetic entropy change in first-order magnetic transition under external fields, J. Alloys Compd. 1017 (2025) 179001.
[7] M.A. McGuire, H. Dixit, V.R. Cooper, B.C. Sales, Coupling of crystal structure and magnetism in the layered, ferromagnetic insulator CrI_3, Chem. Mater. 27 (2) (2015) 612–620.
[8] T. Song, X. Cai, M.W.-Y. Tu, X. Zhang, B. Huang, N.P. Wilson, K.L. Seyler, L. Zhu, T. Taniguchi, K. Watanabe, M.A. McGuire, D.H. Cobden, D. Xiao, W. Yao, X. Xu, Giant tunneling magnetoresistance in spin-filter van der Waals heterostructures, Science 360 (6394) (2018) 1214–1218.
[9] D.R. Klein, D. MacNeill, J.L. Lado, D. Soriano, E. Navarro-Moratalla, K. Watanabe, T. Taniguchi, S. Manni, P. Canfield, J. Fernández-Rossier, P. Jarillo-Herrero, Probing magnetism in 2D van der Waals crystalline insulators via electron tunneling, Science 360 (6394) (2018) 1218–1222.
[10] H.H. Kim, B. Yang, T. Patel, F. Sfigakis, C. Li, S. Tian, H. Lei, A.W. Tsen, One million percent tunnel magnetoresistance in a magnetic van der Waals heterostructure, Nano Lett. 18 (8) (2018) 4885–4890.
[11] Z. Wang, I. Gutiérrez-Lezama, N. Ubrig, M. Kroner, M. Gibertini, T. Taniguchi, K. Watanabe, A. Imamoglu, E. Giannini, A.F. Morpurgo, Very large tunneling magnetoresistance in layered magnetic semiconductor CrI_3, Nat. Commun. 9 (1) (2018) 2516.
[12] C. Lei, B.L. Chittari, K. Nomura, N. Banerjee, J. Jung, A.H. MacDonald, Magnetoelectric response of antiferromagnetic CrI_3 bilayers, Nano Lett. 21 (5) (2021) 1948–1954.
[13] D. Wang, B. Sanyal, Systematic study of monolayer to trilayer CrI_3: Stacking sequence dependence of electronic structure and magnetism, J. Phys. Chem. C 125 (33) (2021) 18467–18473.
[14] H.B. Tran, H. Momida, Y.-i. Matsushita, K. Shirai, T. Oguchi, Insight into anisotropic magnetocaloric effect of CrI_3, Acta Mater. 231 (2022) 117851.
[15] W. Wang, R. Liu, D. Lv, X. Luo, Monte Carlo simulation of magnetic properties of a nano-graphene bilayer in a longitudinal magnetic field, Superlattices Microstruct. 98 (2016) 458–472.
[16] W. Wang, S.-q. Yang, Y. Yang, Z. Peng, B.-c. Li, M. Yang, Magnetic behaviors in a bilayer graphene nanoisland structure: A Monte Carlo study, Phys. E: Low-Dimensional Syst. Nanostructures 109 (2019) 30–38.
[17] H.-j. Wu, W. Wang, B.-c. Li, M. Yang, S.-q. Yang, F. Wang, Magnetic properties in graphene-like nanoisland bilayer: Monte Carlo study, Phys. E: Low-Dimensional Syst. Nanostructures 112 (2019) 86–95.
[18] O.K.T. Nguyen, P.H. Nguyen, N.T. Nguyen, C.T. Bach, H.D. Nguyen, G.H. Bach, Monte Carlo investigation for an Ising model with competitive magnetic interactions in the dominant ferromagnetic-interaction regime, Commun. Phys. 33 (2) (2023) 205.
[19] P.H. Nguyen, G.H. Bach, Thermodynamic properties of the first-order magnetic transition in the highly anisotropic 2D Blume–Capel model, Commun. Phys. 35 (3) (2025) 203–212.
[20] N.T. Nguyen, G.H. Bach, T.H. Pham, H.D. Nguyen, O.T.K. Nguyen, C.T. Bach, Magnetization process in bilayer honeycomb spin lattice, Mater. Trans. 64 (9) (2023) 2118–2123.
[21] K. Hukushima, K. Nemoto, Exchange Monte Carlo method and application to spin glass simulations, J. Phys. Soc. Japan 65 (6) (1996) 1604–1608.
[22] N. Metropolis, A.W. Rosenbluth, M.N. Rosenbluth, A.H. Teller, E. Teller, Equation of state calculations by fast computing machines, J. Chem. Phys. 21 (6) (1953) 1087–1092.
[23] R.H. Swendsen, J.-S. Wang, Nonuniversal critical dynamics in Monte Carlo simulations, Phys. Rev. Lett. 58 (2) (1987) 86–88.
[24] U. Wolff, Collective Monte Carlo updating for spin systems, Phys. Rev. Lett. 62 (4) (1989) 361–364.
[25] J.A. Plascak, A.M. Ferrenberg, D.P. Landau, Cluster hybrid Monte Carlo simulation algorithms, Phys. Rev. E 65 (6) (2002) 066702.
[26] A. Jabar, R. Masrour, A. Benyoussef, M. Hamedoun, Magnetic properties of the mixed spin-1 and spin-3/2 Ising system on a bilayer square lattice: A Monte Carlo study, Chem. Phys. Lett. 670 (2017) 16–21.
[27] R. Masrour, A. Jabar, Magnetic properties of bilayer graphene: a Monte Carlo study, J. Comput. Electron. 16 (1) (2017) 12–17.
[28] M. Karimou, R.A. Yessoufou, G.D. Ngantso, F. Hontinfinde, A. Benyoussef, Mean-field and Monte Carlo studies of the magnetic properties of a spin-7/2 and spin-5/2 Ising bilayer film, J. Supercond. Nov. Magn. 32 (6) (2019) 1769–1779.
[29] N.-x. Li, W. Wang, J.-y. Liu, Z.-y. Xu, C. Xu, J.-l. Yang, Monte Carlo study of magnetic properties of CrI_3-like structure, Micro Nanostructures 181 (2023) 207610.
[30] D. Lv, W. Wang, J.-p. Liu, D.-q. Guo, S.-x. Li, Phase diagrams and magnetic properties of a ferrimagnetic Ising bilayer superlattice: A Monte Carlo study, J. Magn. Magn. Mater. 465 (2018) 348–359.
[31] R. Masrour, L. Bahmad, A. Benyoussef, Size effect on magnetic properties of a nano-graphene bilayer structure: A Monte Carlo study, J. Magn. Magn. Mater. 324 (23) (2012) 3991–3996.
[32] R. Masrour, A. Jabar, Magnetic properties of bilayer graphene armchair nanoribbons: A Monte Carlo study, J. Magn. Magn. Mater. 426 (2017) 225–229.
[33] L. Sun, W. Wang, C. Liu, B.-h. Xu, D. Lv, Z.-y. Gao, The magnetic behaviors and magnetocaloric effect of a nano-graphene bilayer: A Monte Carlo study, Superlattices Microstruct. 149 (2021) 106775.
[34] K. Binder, Finite size scaling analysis of Ising model critical properties, Rep. Progr. Phys. 50 (7) (1987) 783.
[35] D.P. Landau, K. Binder, A Guide to Monte Carlo Simulations in Statistical Physics, third ed., Cambridge University Press, Cambridge, UK, 2009.
[36] N. Chau, N.D. Tho, N.H. Luong, B.H. Giang, B.T. Cong, Spin glass-like state, charge ordering, phase diagram and positive entropy change in $Nd_{0.5-x}Pr_xSr_{0.5}MnO_3$ perovskites, J. Magn. Magn. Mater. 303 (2) (2006) e402–e405.
[37] G.H. Bach, O.K.T. Nguyen, C.V. Nguyen, C.T. Bach, First order magnetization process in polycrystalline perovskite manganite, Mater. Trans. 56 (9) (2015) 1320–1322.
[38] C.T. Bach, T.H. Pham, C.T. Nguyen, Tunnelling magnetoresistance in nanometer granular perovskite systems, J. Phys.: Conf. Ser. 187 (1) (2009) 012007.
[39] D.C. Worledge, T.H. Geballe, Magnetoresistive double spin filter tunnel junction, J. Appl. Phys. 88 (9) (2000) 5277–5279.
[40] G. Kresse, J. Hafner, Ab initio molecular dynamics for liquid metals, Phys. Rev. B 47 (1) (1993) 558–561.
[41] P. Giannozzi, S. Baroni, N. Bonini, M. Calandra, R. Car, C. Cavazzoni, D. Ceresoli, G.L. Chiarotti, M. Cococcioni, I. Dabo, A. Dal Corso, S. de Gironcoli, S. Fabris, G. Fratesi, R. Gebauer, U. Gerstmann, C. Gougoussis, A. Kokalj, M. Lazzeri, L. Martin-Samos, N. Marzari, F. Mauri, R. Mazzarello, S. Paolini, A. Pasquarello, L. Paulatto, C. Sbraccia, S. Scandolo, G. Sclauzero, A.P. Seitsonen, A. Smogunov, P. Umari, R.M. Wentzcovitch, QUANTUM ESPRESSO: a modular and open-source software project for quantum simulations of materials, J. Phys.: Condens. Matter. 21 (39) (2009) 395502.
[42] S. Jiang, J. Shan, K.F. Mak, Electric-field switching of two-dimensional van der Waals magnets, Nat. Mater. 17 (5) (2018) 406–410.
[43] M.A. McGuire, Crystal and magnetic structures in layered transition metal dihalides and trihalides, Crystals 7 (5) (2017) 121.
[44] D. Zhong, K.L. Seyler, X. Linpeng, R. Cheng, N. Sivadas, B. Huang, E. Schmidgall, T. Taniguchi, K. Watanabe, M.A. McGuire, W. Yao, D. Xiao, K.-M.C. Fu, X. Xu, Van der Waals engineering of ferromagnetic semiconductor heterostructures for spin and valleytronics, Sci. Adv. 3 (5) (2017) e1603113.
[45] S. Jiang, L. Li, Z. Wang, K.F. Mak, J. Shan, Controlling magnetism in 2D CrI_3 by electrostatic doping, Nature Nanotechnology 13 (7) (2018) 549–553.
[46] B. Huang, G. Clark, D.R. Klein, D. MacNeill, E. Navarro-Moratalla, K.L. Seyler, N. Wilson, M.A. McGuire, D.H. Cobden, D. Xiao, W. Yao, P. Jarillo-Herrero, X. Xu, Electrical control of 2D magnetism in bilayer CrI_3, Nature Nanotechnology 13 (7) (2018) 544–548.